



Delft University of Technology

Dynamics of a supersonic transitional flow over a backward-facing step

Hu, Weibo; Hickel, Stefan; Van Oudheusden, Bas

DOI

[10.1103/PhysRevFluids.4.103904](https://doi.org/10.1103/PhysRevFluids.4.103904)

Publication date

2019

Document Version

Final published version

Published in

Physical Review Fluids

Citation (APA)

Hu, W., Hickel, S., & Van Oudheusden, B. (2019). Dynamics of a supersonic transitional flow over a backward-facing step. *Physical Review Fluids*, 4(10), Article 103904.
<https://doi.org/10.1103/PhysRevFluids.4.103904>

Important note

To cite this publication, please use the final published version (if applicable).
Please check the document version above.

Copyright

Other than for strictly personal use, it is not permitted to download, forward or distribute the text or part of it, without the consent of the author(s) and/or copyright holder(s), unless the work is under an open content license such as Creative Commons.

Takedown policy

Please contact us and provide details if you believe this document breaches copyrights.
We will remove access to the work immediately and investigate your claim.

Green Open Access added to TU Delft Institutional Repository

'You share, we take care!' - Taverne project

<https://www.openaccess.nl/en/you-share-we-take-care>

Otherwise as indicated in the copyright section: the publisher is the copyright holder of this work and the author uses the Dutch legislation to make this work public.

Dynamics of a supersonic transitional flow over a backward-facing step

Weibo Hu[✉], Stefan Hickel, and Bas van Oudheusden

*Faculty of Aerospace Engineering, Delft University of Technology,
Kluyverweg 1, 2629HS, Delft, The Netherlands*



(Received 4 April 2019; published 17 October 2019)

The transition mechanism and unsteady behavior behind a backward-facing step (BFS) in the supersonic regime at $\text{Ma} = 1.7$ and $\text{Re}_{\delta_0} = 13\,718$ is investigated using large-eddy simulation (LES). The visualization of the flow field shows that the transition process behind the step is initiated by a Kelvin-Helmholtz (K-H) instability of the separated shear layer, followed by secondary modal instabilities of the K-H vortices, leading to Λ -shaped vortices, hair-pin vortices and finally to a fully turbulent state. The separation system features a broadband low-frequency dynamics in the range of $f\delta_0/u_\infty = 0.003 \sim 0.20$ as concluded from the spectral and statistical analysis. Dynamic mode decomposition suggests that the medium frequency motions centered around $f\delta_0/u_\infty = 0.06$ are related to the interactions between reattaching and the shedding of large coherent shear vortices, while the lower ($f\delta_0/u_\infty \approx 0.01$) and higher ($f\delta_0/u_\infty \approx 0.1$) frequency unsteadiness are associated with the periodical expansion and shrinking of the separation system and the convection of upstream K-H vortices, respectively. All these three unsteady mechanisms are coupled to the laminar-to-turbulent transition process in the different stages.

DOI: [10.1103/PhysRevFluids.4.103904](https://doi.org/10.1103/PhysRevFluids.4.103904)

I. INTRODUCTION

The backward-facing step (BFS) is one of the canonical configurations in aerospace applications (e.g., window frame of cockpits, skin joints of fuselage and inlets, flame holder of combustors, etc.), and the flow field over which has attracted extensive attention in the past decades. It is not only an appealing prototype for investigating the separation, recirculation, and reattachment behavior in the view of its geometrical simplicity [1,2] but also for studying the transition from laminar to turbulent flow without artificial disturbances in the nonparallel open flow [3,4].

As it is well known, transition from laminar to turbulent flow is triggered by the instability of the attached or separated shear layer, which can be characterized by the level and growth rate of the unsteady fluctuations. For the subsonic flow case, there is considerable experimental and numerical evidence of the vortex structure behind a BFS. Different from the conventional transition, the dominant instability is not the amplification of Tollmien-Schlichting (T-S) modes in the BFS case [3]. Instead, the involving flow features usually are the large primary eddy as well as Görtler-like and Kelvin-Helmholtz (K-H) vortices [5,6]. Correspondingly, the dominant instability of the transitional flow may be centrifugal forces, lift-up effects or K-H instability depending on the relative step height. For a BFS with sufficiently large step height to boundary layer thickness ratio, the dominant transition mechanism is reported to be the centrifugal forces. Regarding this instability, there is a large primary eddy behind the step with almost circular streamlines at the center of the separation bubble. Most of the kinetic energy is observed at the downward side of the shear flow, where streamline curvature and the corresponding centrifugal forces are significant [7]. With respect to a

*W.Hu-2@tudelft.nl

BFS with a small expansion ratio at low Reynolds number, the incoming perturbations are amplified in the separated shear layer behind the step because of the inviscid instability and the induced three-dimensional disturbances evolve into longitudinal streaks downstream the separation bubble. These large coherent structures are caused by the lift-up effects, where low-speed fluid is lifted up near the wall and ejected into the upper regions (upwash), while the high-speed fluid is transported to the lower part of the shear layer from the main flow (downwash). These Görtler-like vortices are self-sustained due to the feedback provided by recirculating flow in the separation bubble [7]. The expected K-H instability was not observed by Tinney and Ukeiley [8] due to the short residence time of flow in the shear layer. However, experimental work of Duncan Jr [9] shows that there exists a critical step height as a function of unit Reynolds number, beyond which the traveling and shedding of the K-H vortices is the main incentive of the transition process, see also [10]. The classical transition path consist of the roll-up of the shear layer, the convection of quasi-periodic K-H vortices, flapping motion of the reattachment and separation bubble, as well as the vortex breakdown to turbulence [11]. Furthermore, Eppink *et al.* [12] observed a modulation mechanism in their experimental study of a case with crossflow. In their opinion, the acceleration of the transition over the BFS is the result of the interactions of various instabilities, including low-frequency traveling waves, medium-frequency T-S modes and high-frequency shear layer instability. In addition, the interaction between separation and transition results in the low-frequency unsteadiness of the recirculation system whose frequency usually is two orders lower than that of the inflow boundary layer and believed to be associated with the quasi-periodic motions of the separation bubble [13]. In conclusion, it appears that the nonlinear instability, rather than the linear growth of T-S waves, plays a more important role in the transition process behind a BFS [14].

For the supersonic regime, stability analysis also shows a strong shear-layer induced instability featured with a large frequency range in the separation region [15]. However, there are probably additional mechanisms involved, that are related to compressibility and the occurrence of compression waves at flow reattachment [16,17]. Therefore, it is reasonable to conjecture that a different mechanism may contribute to the transition process in the supersonic case. Yi *et al.* [18,19] inferred from their flow visualization that the unsteadiness of the separation system depends on compressibility and K-H vortices of the shear layer rather than the restriction effects of the wall or the reattachment events. Additionally, a broadband oscillation dynamics was also found in recent experiments with low-level turbulent inflow using particle image velocimetry (PIV) [20]. Compared to the subsonic case, significant lower frequency motions are observed within the recirculation zone.

In the present work, we investigate the flow field behind an open BFS configuration to enhance our understanding of the self-excited transition process and the unsteady features of the interaction system in the supersonic flow, especially the effects of shock waves and interactions between different unsteady mechanism, using large eddy simulation (LES). In Sec. II, a detailed description of the flow configuration and numerical method is provided. Section III first analyzes the transition process of the shear flow by examining the mean and instantaneous flow structure. Then the effects of shock and reattachment on the transition are inspected by spectral and statistical analysis. Finally, the dominant modes in the evolution of the transitional flow are discussed using dynamic mode decomposition (DMD). The conclusions with a summary of main results and a model for the physical mechanisms are presented in Sec. IV.

II. FLOW CONFIGURATION AND NUMERICAL SETUP

A. Flow configuration

The setup for the present study is an open BFS (no upper wall) with a supersonic laminar inflow, a schematic of which is shown in Fig. 1. With this configuration, we can remove the effects of wave reflections from the upper wall and resonator dynamics between upstream perturbations and shear layer.

The laminar inflow is characterized by the free-stream Mach number $\text{Ma}_\infty = 1.7$ and the Reynolds number $\text{Re}_{\delta_0} = 13\,718$ based on the inlet boundary layer thickness δ_0 (at 99% u_∞) and

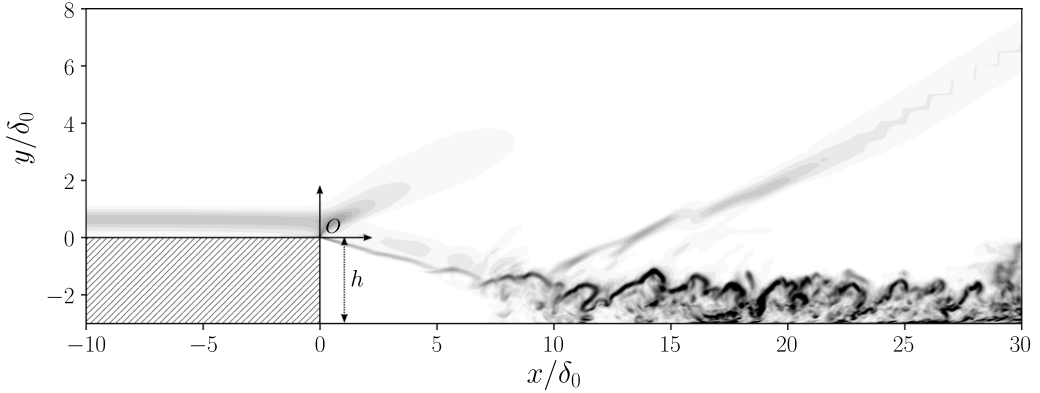


FIG. 1. Schematic of the region of interest, which is in the center of the large computational domain with the size of $([-40, 70] \times [-3, 30] \times [-2.5, 2.5])\delta_0$ in the x , y , z directions. The solid box contains an instantaneous numerical schlieren graph in the x - y cross section.

free-stream velocity u_∞ . Main flow parameters are summarized in Table I. We indicate free stream flow parameters with subscript ∞ and stagnation parameters with subscript 0. The size of the computational domain is $[L_x, L_y, L_z] = [110\delta_0, 33\delta_0, 5\delta_0]$ including a length of $40\delta_0$ upstream the step to exclude potential uncertain effects from the numerical inlet boundary conditions on the flow in the region of interest. The height of the step is three times larger than the inlet boundary layer thickness, which is large enough to induce the transition from laminar to turbulent flow [9].

B. Numerical setup

We employ the implicit LES method of Hickel *et al* [21] for solving the compressible Navier-Stokes equations. The subgrid scale model is fully merged into the numerical scheme provided by the adaptive local deconvolution method (ALDM) [21,22]. The viscous flux is discretized by a second-order central difference scheme and an explicit third-order total variation diminishing (TVD) Runge-Kutta scheme [23] is used for time marching. This method has been successfully applied to various supersonic flow cases, including shock wave/boundary layer interaction (SWBLI) on a flat plate [24] and compression ramp [25], and transition between regular and irregular shock patterns in SWBLI [26]. More details about the numerical method can be found in Hickel *et al.* [21].

For the spatial discretization, a Cartesian grid structure with block-based local refinement was applied for the entire domain, as displayed in Fig. 2. In addition, hyperbolic grid stretching was used in the wall-normal direction downstream of the step. Upstream of the step, the near wall grids are distributed uniformly. The mesh is sufficiently refined near all walls to ensure a well-resolved wall shear stress. The grid spacing becomes coarser with increasing wall distance but the expansion ratio is not larger than two. Using this discretization strategy, the computation domain has around 8.47×10^6 cells; thus we obtain a spatial resolution of the flow field with $\Delta x_{\max}^+ \times \Delta y_{\max}^+ \times \Delta z_{\max}^+ = 0.9 \times 1.0 \times 20$ for the flow domain, except the singular region at the step corner. The temporal resolution, that is the time step, is approximately $\Delta t u_\infty / \delta_0 = 7.6 \times 10^{-4}$, corresponding to a Courant-Friedrichs-Lowy condition $CFL < 0.5$.

TABLE I. Main flow parameters of the current case.

Ma_∞	U_∞	δ_0	θ_0	δ_0^*	Re_∞	T_0	p_0	h	p_∞
1.7	469.85 m/s	1 mm	0.107 mm	0.479 mm	$1.3718 \times 10^7 \text{ m}^{-1}$	300 K	$1 \times 10^5 \text{ Pa}$	3 mm	20259 Pa

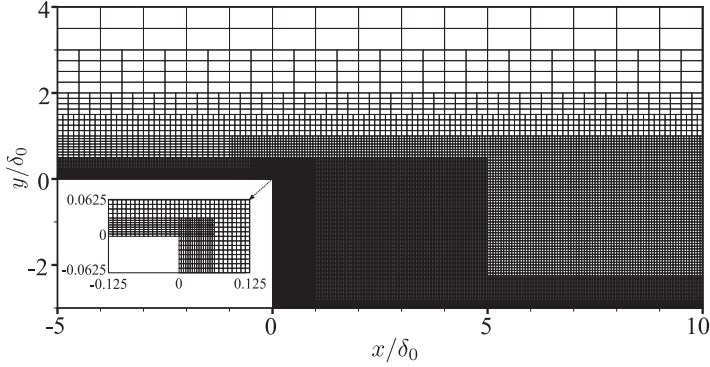


FIG. 2. Grid distribution in the x - y plane in the computational domain near the step.

The dynamic viscosity μ and thermal conductivity κ used in the current calculation are the function of static temperature by Sutherland's law and Prandtl number Pr

$$\mu = \mu_{\text{ref}} \frac{T_{\text{ref}} + S}{T + S} \left(\frac{T}{T_{\text{ref}}} \right)^{1.5}, \quad \kappa = \frac{c_p \mu}{\text{Pr}}, \quad (1)$$

where $\mu_{\text{ref}} = 18.21 \times 10^{-6}$ Pa s, $T_{\text{ref}} = 293.15$ K, $S = 110.4$ K, $\text{Pr} = 0.72$ and $c_p = 1004.7$ J/(kg K). At the domain inlet, a clean compressible laminar boundary profile is imposed. The step and wall are modeled as nonslip adiabatic surfaces. All the flow variables are extrapolated at the outlet of the domain. On the top of the domain, nonreflecting boundary conditions based on Riemann invariants are used. Periodic boundary conditions are imposed in the spanwise direction.

For the current computations, the time- and spanwise-averaged statistics were sampled at every $t u_\infty / \delta_0 = 0.5$. We simulated an initial period of $t u_\infty / \delta_0 = 500$, during which the flow reached a fully developed statistically steady state. After this initial transient, statistics were sampled over another $t u_\infty / \delta_0 = 800$. The van Driest transformed mean velocity profile was plotted at a streamwise station downstream the reattachment point (at $x/\delta_0 = 30.0$ where $\text{Re}_\tau = 715$) in Fig. 3.

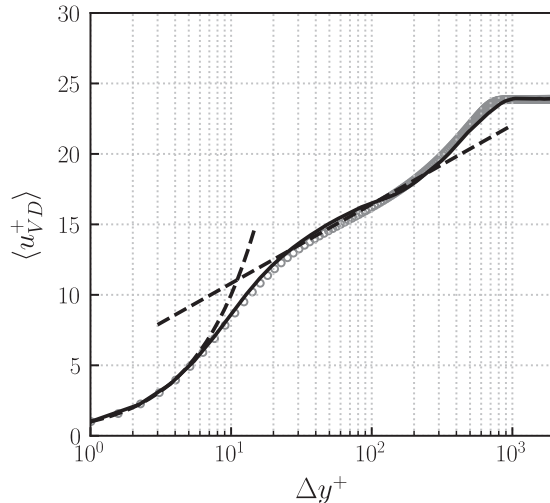


FIG. 3. Van Driest transformed mean velocity profile at $x/\delta_0 = 30.0$. -----, law of the wall; ——, present LES; ○, incompressible DNS data of Schlatter at $\text{Re}_\tau = 671$ [27].

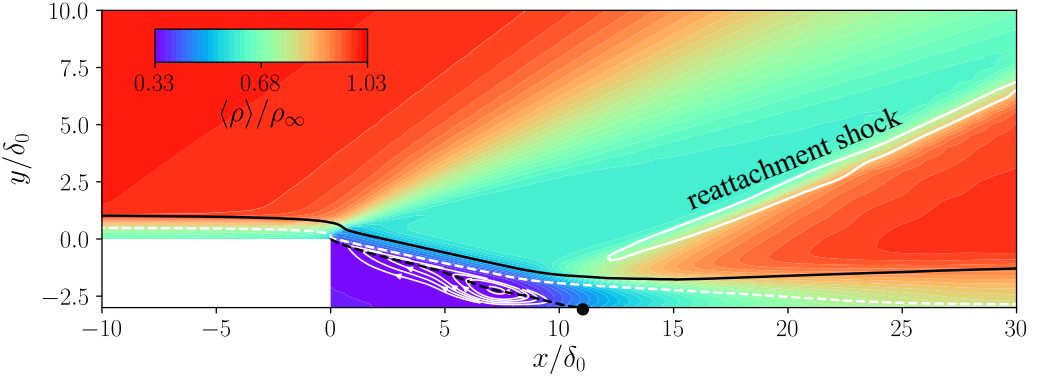


FIG. 4. Time and spanwise-averaged contour of density with isolines of streamwise velocity and Mach number. A solid circle (\bullet) indicates the reattachment point. The white dashed and solid lines denote the isolines of $\text{Ma} = 1.0$ and $|\nabla p|/\delta_0/p_\infty = 0.24$. The black dashed and solid lines signify isolines of $u = 0.0$ and $u/u_e = 0.99$.

The theoretical results and incompressible DNS data of Schlatter [27] at $\text{Re}_\tau = 671$ are also included for the comparison. Although the turbulent boundary layer downstream the separation bubble has not reached a fully equilibrium state yet, the present mean velocity profile is in very good agreement with both the logarithmic law of the wall (with the constants $\kappa = 0.41$ and $C = 5.2$) and DNS results. To verify grid convergence and domain size independence, the same calculation was carried out with a spanwise length $z/\delta_0 = 16.0$ (3.2 times larger than the current one) and a finer grid, which resulted in very similar instantaneous flow structures and the same mean velocity profiles.

III. RESULTS

A. Mean flow visualization

The main flow features are visualized by the time- and spanwise-averaged density contours shown in Fig. 4. The incoming laminar flow experiences a centered Prandtl-Meyer expansion when it separates at the step corner due to the sudden geometry expansion. Then the free shear layer develops towards the downstream wall and finally impinges on the wall surface. Compression waves are generated around the reattachment location, which coalesce into a reattachment shock (white solid line). The low-speed recirculating flow forms a separation bubble underneath the dividing line (here defined for convenience as the isoline of $u = 0$ indicated by black dashed line), while the high-speed part proceeds downstream by overcoming the slight pressure rise [28]. The mean reattachment length is about $L_r = 10.9\delta_0$ ($3.6h$), which is consistent with the existing results, reporting that the reattachment length is usually within $3.0 \sim 4.0h$ around the current Mach number [28,29]. Behind the reattachment point, the distance between the sonic line (white dashed line) and wall decreases with the streamwise distance as a result of the increasing velocity gradient near the wall, which indicates the evolution towards a fully turbulent boundary layer. The reattachment length $L_r = 3.6h$ is much smaller than the typical values reported for incompressible cases (e.g., $19.8h$ [11]) due to the more energetic mixing of the shear layer with the increasing Reynolds number. This interpretation is in accordance with the finding that the reattachment length is reduced with the Reynolds number in the transitional regime [30].

The reattachment length is further confirmed by the mean skin friction distribution in Fig. 5(a), where $\langle C_f \rangle$ represents the skin friction normalized by $0.5\rho_\infty U_\infty^2$. The intensity of separated flow is not uniform in terms of $\langle C_f \rangle$, varying with streamwise distance along the separation bubble. The level of $\langle C_f \rangle$ remains almost zero in the upstream part of the separation bubble ($0 < x/\delta_0 < 6.3$),

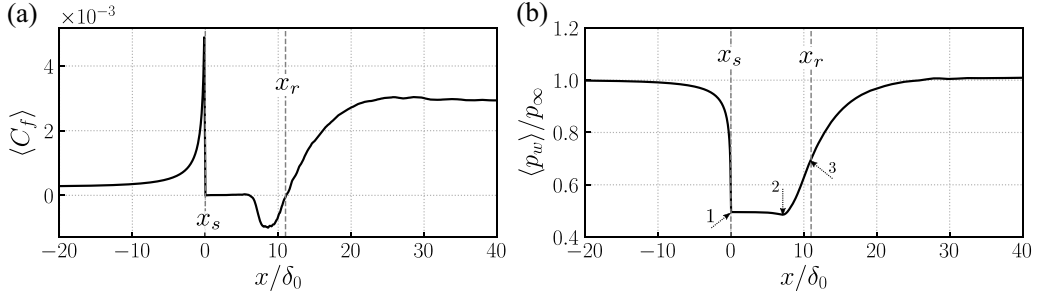


FIG. 5. Time- and spanwise-averaged (a) skin friction and (b) wall pressure. The dash line indicates the averaged separation and reattachment location.

which is followed by a decrease of $\langle C_f \rangle$ towards a global minimum at $x/\delta_0 = 8.4$. Then $\langle C_f \rangle$ slowly climbs up and eventually stays steady at about $\langle C_f \rangle = 2.9 \times 10^{-3}$ for $x/\delta_0 > 25$, which is a typical level of the turbulent boundary layer at the current Reynolds number range. The trend and level of $\langle C_f \rangle$ match well with the numerical results of Spazzini *et al.* [13] despite the different inlet boundary conditions and reattachment length. As will be shown later, this structure of $\langle C_f \rangle$ inside the recirculating region seems to be related to the low-frequency unsteadiness.

The wall pressure in Fig. 5(b) displays a sharp drop by about 50% in front of the step. The wall pressure then gradually reduces further to reach its global minimum at $x/\delta_0 = 7.3$ in the separation bubble. In terms of the trend and relative variation, our results are in good agreement with the numerical works of Karimi *et al.* [29]. The three inflection points of the wall-pressure distribution are considered to be associated with the separation, emergence of compression waves and reattachment, as reported in Ref. [31].

The boundary layer state can be characterized basically by the evolution of the wall-normal velocity profile along the streamwise direction, see Fig. 6, where $\Delta y/\delta_0$ signifies the normalized wall distance. Sufficiently upstream of the step edge, the velocity profile corresponds to a typical laminar boundary layer. At the step corner ($x/\delta_0 = 0$), the streamwise velocity gradient increases significantly due to the upstream effect of the sharp expansion of the geometry. Accordingly, the boundary layer thickness gradually decreases along the streamwise distance upstream the step (see Fig. 4). It is noticeable that there exists an inflection point of the velocity profile at this location,

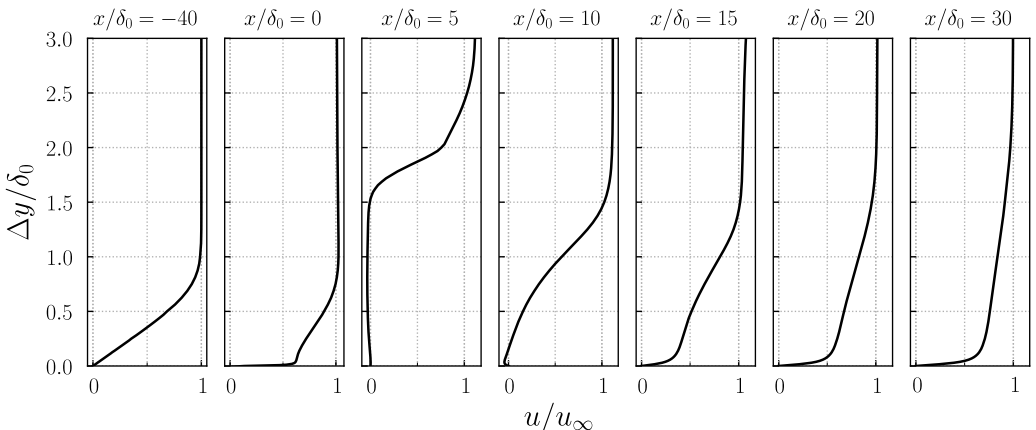


FIG. 6. Streamwise evolution of spanwise and time-averaged streamwise velocity profile. Note: the y axis is the nondimensional normal distance from the wall.

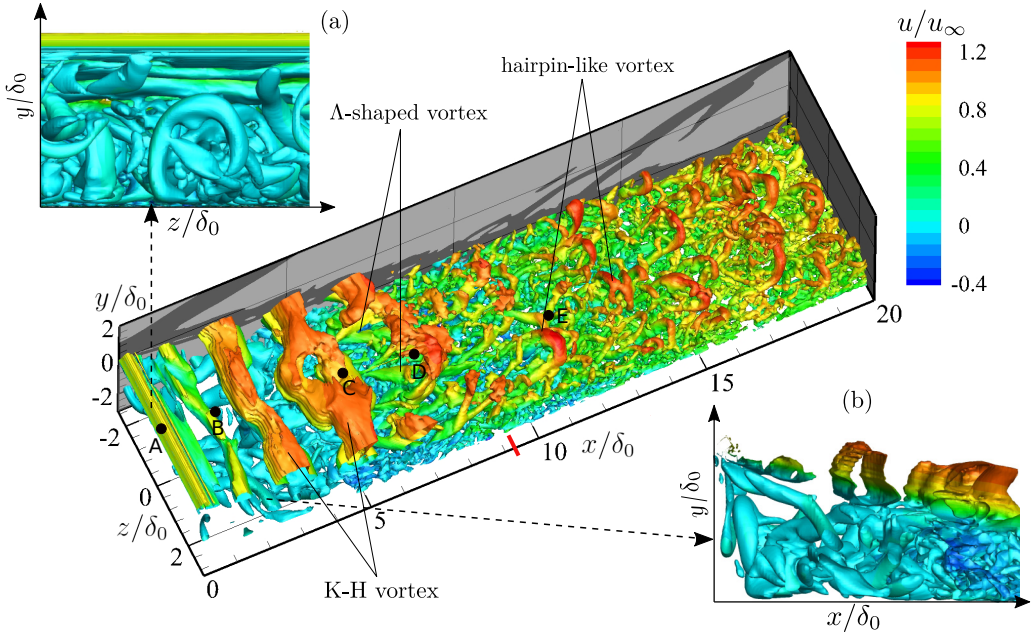


FIG. 7. Instantaneous vortical structures at $tu_\infty/\delta_0 = 793$, visualized by isosurfaces of $\lambda_2 = -0.005$. The black shade represents the contour of $|\nabla p|/\delta_0/p_\infty = 0.24$ at the slice $z/\delta_0 = -2.5$. The red solid line signifies the instantaneous spanwise-averaged reattachment point. (a) The ejection behavior; (b) the streamwise vortices.

which means that the boundary layer has an inviscid instability at the step. The mean streamwise velocity increases across the expansion due to the favorable pressure gradient [see also Fig. 5(b)]. Compared to the upstream velocity profile, the boundary layer profile displays a large momentum deficit in the separated region, for example, at $x/\delta_0 = 5$ there is only a small reverse flow region, however, the velocity deficit of $1.0u_\infty$ extends up to around $\Delta y/\delta_0 = 1.5$. Also shortly downstream of reattachment (which takes places near $x/\delta_0 = 11$), the shape of the velocity profile, at $x/\delta_0 = 15$ and $x/\delta_0 = 20$, has not yet reached an equilibrium state. The outer flow velocity gradually returns to its initial level with the adverse pressure gradient behind the reattachment shock, see Fig. 5(b). The flattening of the velocity profile and steeper velocity gradient near the wall, compared to the upstream velocity profile, both indicate the development of the turbulent boundary layer.

B. Instantaneous flow visualization

The instantaneous vortical structures in a typical instantaneous flow realization are visualized by means of the λ_2 vortex criterion, providing an overall view in Fig. 7 and a zoom-in view in Fig. 8. The laminar-to-turbulent transition process can be divided into five stages based on the appearance of the vortical structures. The first stage is the relatively short range where two-dimensional spanwise structures are initiated due to the inviscid K-H instability of the shear layer, as shown in Fig. 8(a).

In the second stage, the spanwise structures evolve further into large quasi two-dimensional vortices [Fig. 8(b)]. These spanwise-aligned K-H vortices are subsequently deforming into oblique waves as a result of their secondary instability, probably triggered by small horseshoe vortices beneath as the free shear layer flow develops downstream.

The streamwise velocity is not distributed uniformly along the oblique waves, which induces the formation of low and high momentum zones along the spanwise direction. With the spanwise modulation of the vortices, the low-momentum parts form into the legs of a Λ -shaped vortex

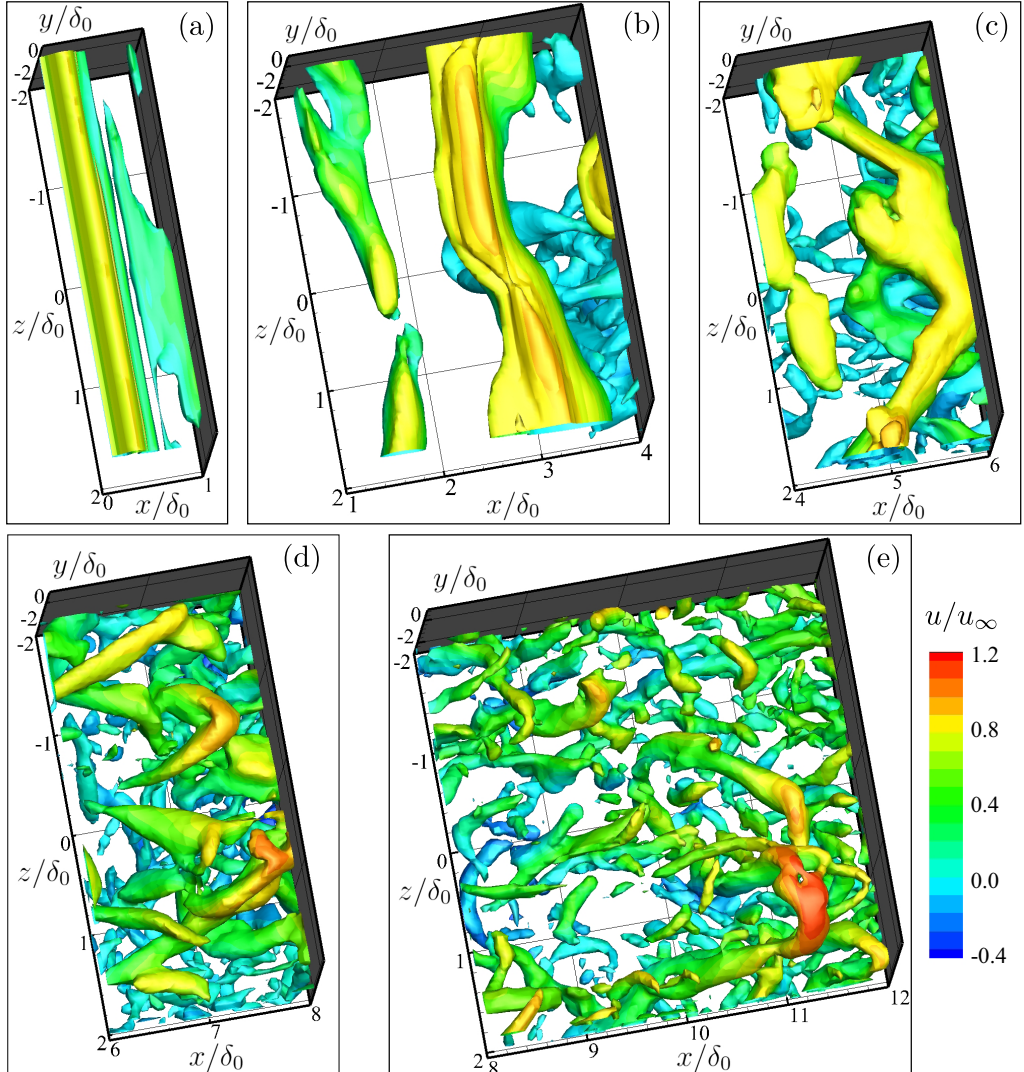


FIG. 8. Instantaneous vortical structures at $tu_\infty/\delta_0 = 793$, colored by contours of streamwise velocity, visualized by isosurfaces of (a) $\lambda_2 = -0.005$, (b) $\lambda_2 = -0.005$, (c) $\lambda_2 = -0.02$, (d) $\lambda_2 = -0.1$, and (e) $\lambda_2 = -0.5$.

structure and the high-momentum parts develop into the head of a Λ -shaped vortex in the third stage; see Fig. 8(c). At the same time, the distorted vortices pair with each other since the high-speed part of upstream vortices catch up with the low-speed part of downstream vortices. The separated shear layer flow thus exhibits the formation of large-scale vortices via K-H and secondary instability, and then these vortices keep stretching, pairing as the shear layer evolves. In the incompressible case of Schäfer *et al.* [11], the vortex pairing is not observed and thus the K-H vortices keep aligned in the spanwise direction upstream of the reattachment point. However, the convection of the K-H vortices is faster in the supersonic flow, which makes it more likely for the high-speed part of the upstream vortices to reach the slow part of the following vortices and to promote the mixing of the shear layer. Existing experimental results have confirmed the behavior of the vortex pairing in the supersonic

laminar flow [19]. However, if the separation length is too short, like in supersonic turbulent flow, there is not enough resident time for K-H vortices to grow and pair within the shear layer.

In the next stage, the large coherent Λ -shaped vortices break down into several small Λ -shaped vortices staggered in the spanwise direction due to the streamwise stretching of vortices, in which the head part of the vortex (relatively far away from the wall) is convected faster than the leg parts until this behavior tears down the large vortex [Fig. 8(d)]. Emerging smaller Λ -shaped vortices indicate the onset of the nonlinear regime, which originates from the upstream self-excited quasi-periodical K-H vortices, instead of the natural spanwise differential amplification of the Tollmien-Schlichting waves [32]. There also exist low-momentum zones in leg parts and high-momentum zones in head parts of the small Λ -shaped vortices.

In the last stage, the vortex-stretching mechanism continues and the hairpin vortices appear to be lifted up due to the stretched legs [33,34]. This rolling up contributes to the formation of large hairpin vortices, which is the signature of turbulent boundary layer flow, illustrated in Fig. 8(e).

We do not observe Görtler vortex pairs from the visualizations of the vortical structure. This suggests that the Görtler instability may not be a predominant mechanism in the transition. We evaluated the Görtler number G_t to quantify the development of the Görtler instability along the streamwise distance to provide more physical evidence. The characteristic Görtler number G_t is defined as

$$G_t = \frac{\theta}{0.018\delta^*} \sqrt{\frac{\theta}{R}}, \quad (2)$$

where δ^* , θ , and R signify the local displacement thickness, the momentum thickness and the curvature radius along a specific streamline, respectively. When the local Görtler number exceeds the critical value $G_t = 0.58$ for a wide range of compressible laminar flow conditions, Görtler vortices will emerge in the boundary layer [24,35]. We computed the value of the local Görtler number along the boundary layer edge and found that it remains below this threshold at every x coordinate as far downstream as the mean reattachment location, where significant turbulence is already observed. Based on the combined evidence of vortical visualizations and the analytical values, we conclude that the Görtler instability does not play an important role in this transitional case.

For each stage of the transition process, spanwise profiles of the fluctuations of the streamwise velocity are shown in Fig. 9 (note the smaller scale for the first two stations). We can clearly see the differences of dimensional features of the traveling waves in each stage. In the first stage, the spanwise waves are completely two-dimensional, and their wavelength is about half of the spanwise domain size, Fig. 9(a). Then these two-dimensional waves modulate into oblique waves and their amplitudes increase by approximately one order, Fig. 9(b). The three-dimensional features of unstable waves are obvious and their fluctuations becomes more energetic in the following three stages. As reviewed by Herbert [36], the vortex pairing process is usually observed in inflectional boundary layers at very large amplitudes of the periodic modulation. It seems that the three-dimensional characteristics of the unstable waves emerge in a very short distance behind the step and soon become highly energetic before reaching half of the reattachment length.

The root-mean square (RMS) and amplification factor of the streamwise velocity fluctuations are plotted as function of the streamwise distance through the five stages of the transition in Fig. 10. Based on the profile of streamwise velocity RMS at a specific x_i location, we find y_i where the local profile has the maximum. The position (x_i, y_i) is considered to be the local most unstable point and computed along the streamwise direction. The RMS of the streamwise velocity we display (solid line in Fig. 10) are the results at these locations (x_i, y_i) . Then we compute the perturbation amplitudes A_i from the time series data at (x_i, y_i) . The amplification factor is normalized based on the amplitude A_0 at $x = 0$. The level of fluctuations grows smoothly in the first two stages and experiences an accelerated growth caused by the secondary instability and vortex breakdown in the third and fourth stage (solid line in Fig. 10). The streamwise modulation of low and high momentum parts of Λ -shaped vortices also contributes to the accelerated growth. In the last stage,

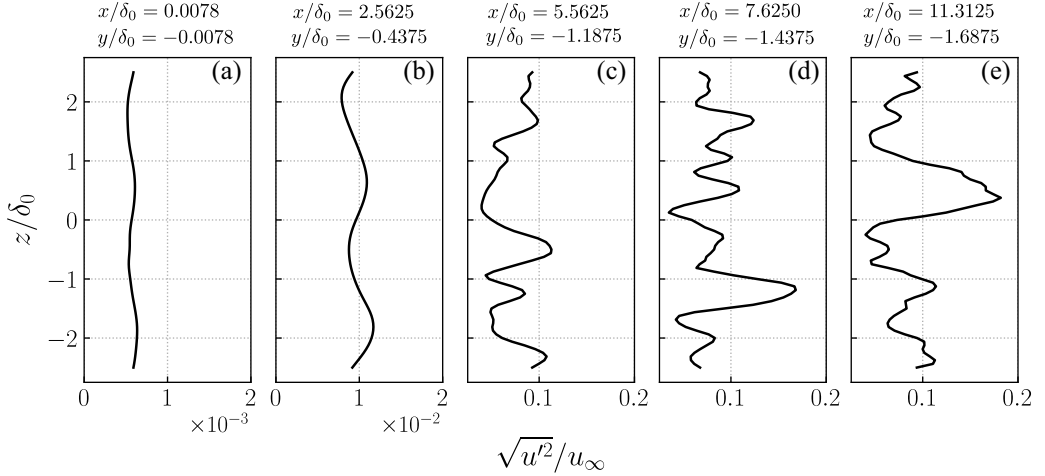


FIG. 9. Fluctuations of streamwise velocity along the spanwise direction at five different locations shown in Fig. 7 (marked as A, B, C, D, and E, each of which corresponds to one stage of the transition process in Fig. 8).

the fluctuations reach their maximum around the reattachment point and return to an almost constant level in the turbulent boundary layer (not shown in the figure). Concerning the amplification factor (dashed line in Fig. 10), at first, the amplitude of fluctuations displays a rapid modal growth of K-H vortices. In the next two stages, the growth rate (presented by the slope of the amplification factor) is much smaller than before although the amplification factor still slowly increases. Then the amplification factor continues increasing because of a rapid onset of nonlinear distortion and breakdown to turbulence in the fourth stage. In the last stage, the amplification factor almost keeps steady at a high level.

In conclusion, the above visualization and analysis show rapid modal growth of K-H type transition right behind the step. The amplitude of fluctuations exceeds $0.1\%u_\infty$ after a short distance from the step, which indicates that nonlinear interactions become important. Therefore, we believe the transition process consists of onset and modal growth of K-H vortices (stage 1, 2), secondary instability (stage 3), breakdown of the large coherent vortices (stage 4), and turbulent state (stage 5).

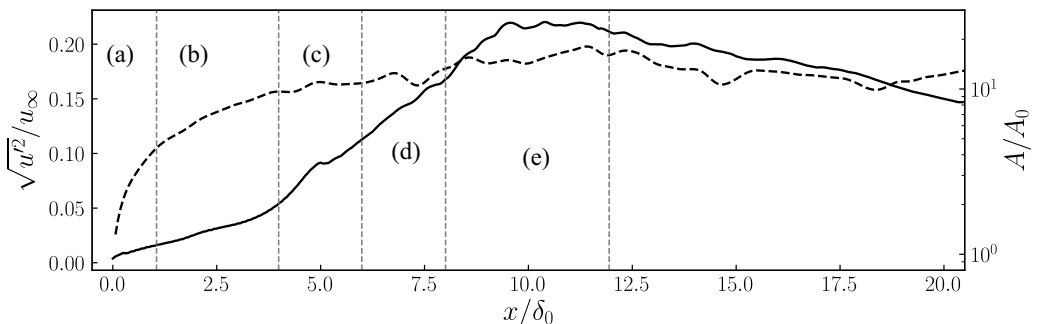


FIG. 10. RMS (solid line) and amplification factor (dashed line) of streamwise velocity fluctuations along streamwise direction through the five stages of the transition in Fig. 8 based on the spanwise-averaged flow field.

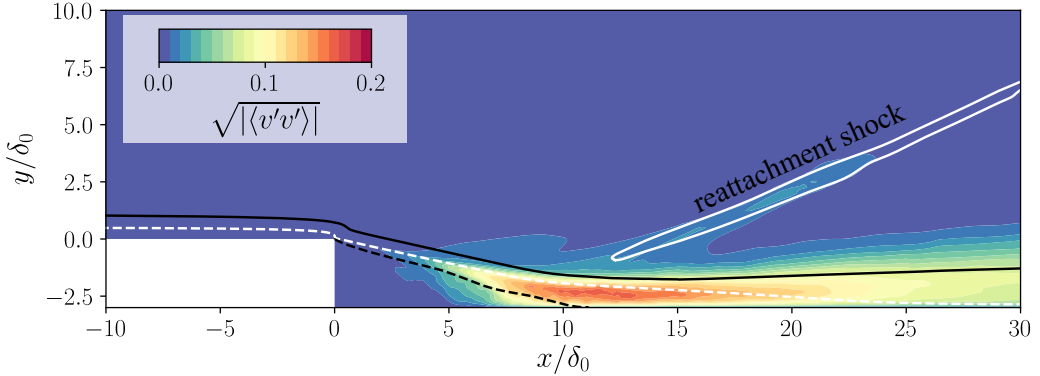


FIG. 11. Contours of the variance of the wall-normal velocity. The white dashed and solid line denote the isolines of $\text{Ma} = 1.0$ and $\nabla p = 0.24$. The black dashed and solid line signify isolines of $u/u_e = 0.0$ and $u/u_e = 0.99$.

C. Unsteady behavior

The unsteadiness of the flow field is examined to find the most energetic mechanism in the laminar-to-turbulent transition. First, the map of RMS values for the wall-normal velocity fluctuations is considered, as plotted in Fig. 11. We do not see any energetic activity upstream the step. The velocity fluctuations are only noticeable starting from the separated shear layer and reach a global maximum around the reattachment region. In addition, relatively small fluctuations are observed in the reattachment shock area, which is likely indication of the unsteadiness of the shock position.

We analyze the dynamic behavior by means of the frequency weighted power spectral density (FWPSD) of the pressure along the dividing line in Fig. 12. Note that all values of FWPSD have been normalized by the local integral values $\int P(f)df$ to better highlight the relative local contributions at different frequencies, independent of the overall fluctuations strength. As we can see in Fig. 12, in the first stage, the separated shear layer features a significant low-frequency oscillation with $f\delta_0/u_\infty \approx 0.02$ immediately behind the step. This unsteady behavior is believed to be associated with the breathing motion of the separation bubble, as we will discuss in the following section. The dominant frequency then shifts towards higher values of $f\delta_0/u_\infty \approx 0.2$ in the second stage where the oblique K-H vortices are observed. Although we can infer that there is still low-frequency

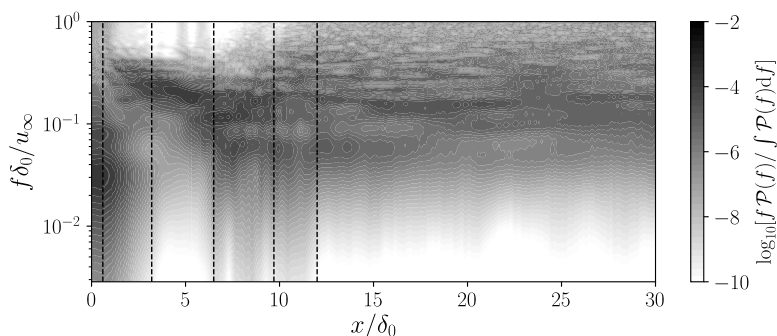


FIG. 12. Frequency weighted power spectral density map of pressure signals along the dividing line based on $z = 0$ slice. At every streamwise location the weighted spectra are normalized by $\int P(f)df$. The five stages of the transition process are indicated by vertical dashed lines.

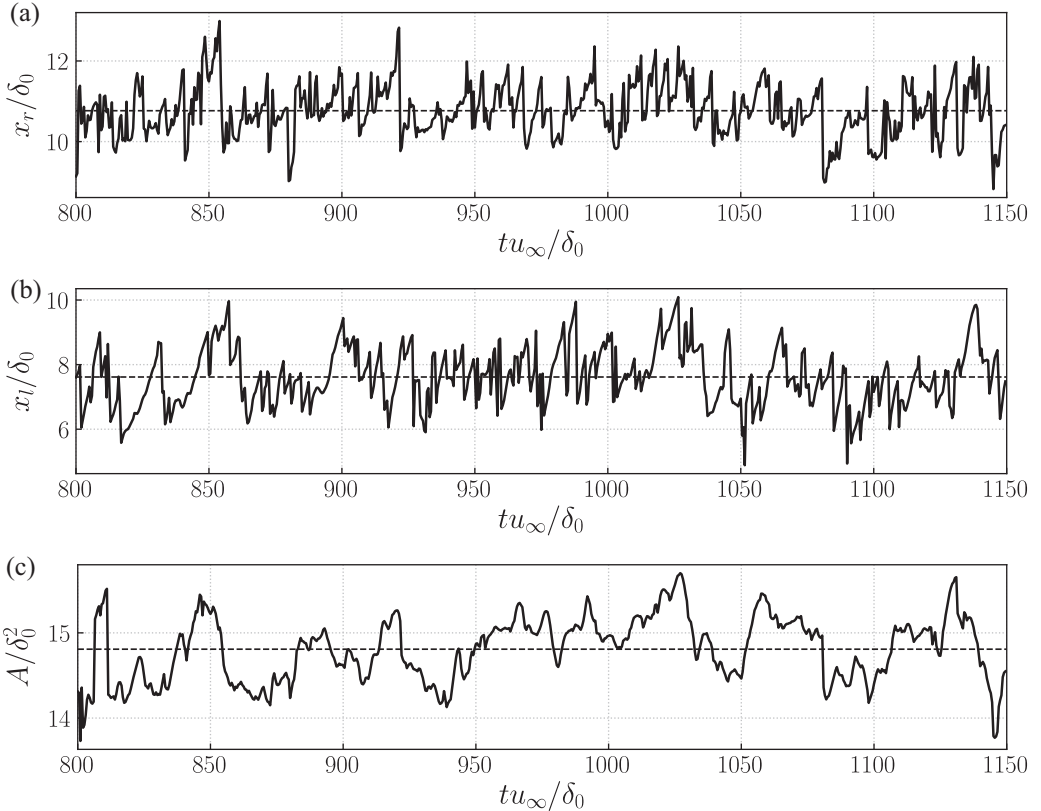


FIG. 13. Temporal variation of the spanwise-averaged (a) reattachment point, (b) shock location, and (c) separation bubble. The dashed line denotes the mean value.

breathing unsteadiness in this stage, the dominant frequency is around the characteristic frequency of the K-H vortices, which underlines the important role of the K-H instability in the transition scenario. As the shear layer develops, the energetic content of the shear layer gradually shifts to lower frequencies in the following stages ($3.2 < x/\delta_0 < 12$) and evolves towards a broadband frequency spectrum from the low to high frequency. Downstream the transition region ($x/\delta_0 \geq 12$), the fluctuations in the turbulent boundary layer are distributed over the spectrum without a clear preferred frequency.

Time signals of three aerodynamic parameters are shown in Fig. 13 to further characterize the unsteady behavior of the interaction, including the spanwise-averaged reattachment point x_r , the reattachment shock location x_l and the cross-sectional area of the separation bubble x_b . The value of x_r is computed as the intersection of the dividing line (isoline of $u = 0$) and the wall in the range from $x/\delta_0 = 8.5$ to 13.5. The separation bubble area x_b is the area of the zone below the dividing line. The shock location x_l is determined based on the pressure gradient outside the boundary layer by fitting the isolines of $|\nabla p| \delta_0 / p_\infty = 0.24$. We obtain two x values by intersecting the isolines of $|\nabla p| \delta_0 / p_\infty = 0.24$ at $y/\delta_0 = 0.0$ and then take the average of these two x values as the first streamwise coordinate of shock position. A second point of the shock position is obtained by repeating the same operation at $y/\delta_0 = 5.0$. A straight line is fitted based on these two points and the intersection between the fitting line and wall is considered as the shock location x_l . A similar method of obtaining these parameters has been applied to investigate SWBLI [37,38].

These temporal signals are extracted in time ranges $t u_\infty / \delta_0 = 800 \sim 1150$ with a sampling frequency $f_s \delta_0 / u_\infty = 2$ as the frequencies above the characteristic frequency of the turbulent

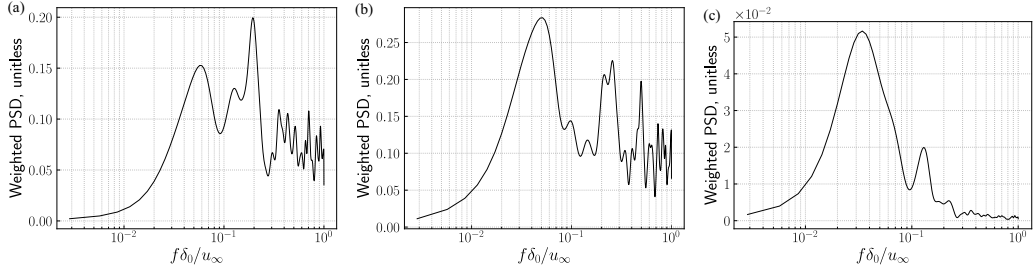


FIG. 14. Frequency weighted power spectral density of the spanwise-averaged (a) reattachment point, (b) shock location, and (c) separation bubble size.

integral scales u_∞/δ_0 are not of the current interest. All these signals include broadband frequency scales because all the plots are irregular and aperiodic. The curve of the reattachment position in Fig. 13(a), displays an almost instantaneous drop when it moves upstream, for example at around $t u_\infty/\delta_0 = 924$. When the reattachment location shifts downstream, it experiences a less rapid relaxation. This sawtooth-like trajectory of the reattachment point was also reported in direct numerical simulation (DNS) results of a compression ramp by Priebe and Martin [38]. The dynamics of the shock location, Fig. 13(b), is slightly smoother, without such strong sawtooth-like behavior. The passage of large-scale vortices in the shear layer and their shedding into the downstream flow contributes to sawtooth-like motions [39,40]. In terms of the separation bubble size, shown in Fig. 13(c), its temporal behavior seems more periodical, with the absence of high-frequency fluctuations.

The FWPSD for the three signals are shown in Fig. 14. The spectra of reattachment and shock location both have two narrow-band peaks around $f\delta_0/u_\infty = 0.06$ and 0.2 . For the reattachment point, Fig. 14(a), most of the energy is contained at $f\delta_0/u_\infty = 0.2$, near the characteristic frequency of the K-H vortices. The K-H frequency $f\delta_0/u_\infty = 0.2$ is in good agreement with the incompressible data of Schäfer *et al.* [11], which, however, does not show the second peak around $f\delta_0/u_\infty = 0.06$. We thus conclude that the lower-frequency content is a characteristic compressible feature due to the occurrence of the compression waves. As for the shock position in Fig. 14(b), the spectrum peaks are located at around $f\delta_0/u_\infty = 0.06$, while the oscillation of the separation bubble has a single dominant frequency peak at $f\delta_0/u_\infty \approx 0.03$ displayed in Fig. 14(c), which is two orders of magnitude lower than the characteristic frequency of the energetic turbulent scales u_∞/δ_0 , in agreement with the widely reported low-frequency unsteadiness in SWBLI [25,41,42]. The experimental work of supersonic BFS flows reported two types of low frequencies centered at $f\delta_0/u_\infty \approx 0.02$ and $f\delta_0/u_\infty \approx 0.05$ [20], which is very close to our current results.

D. Statistical analysis

Three distinct dominant frequencies of the unsteady motions in the interacting system are identified in the previous section. To explore their origin, the statistical connections between the reattachment point and several signals, including pressure fluctuations induced by K-H vortices, shock location, and the area of separation bubble, are investigated using the temporal correlation coefficient R_{ij} between two signals q_i and q_j with time delay, defined as

$$R_{ij}(\Delta t) = \frac{\text{Cov}[q_i(t), q_j(t + \Delta t)]}{\sigma_i \sigma_j}, \quad (3)$$

where Cov is the covariance between these two signals and σ indicates the population standard deviation of the specific signal.

The correlation between the reattachment point and pressure fluctuations of the K-H vortices is shown in Fig. 15(a). The pressure signals used are obtained at the same location of B in Fig. 7;

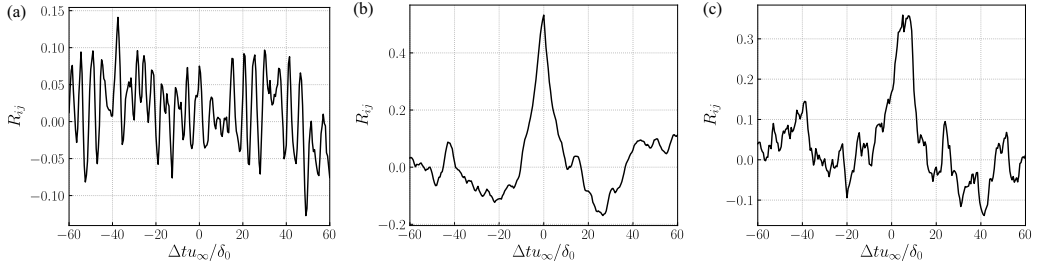


FIG. 15. Temporal cross-correlations between the spanwise-averaged reattachment location and (a) pressures fluctuations upstream the shear layer, (b) separation bubble area, and (c) shock location.

i.e., $x/\delta_0 = 2.5625$, $y/\delta_0 = -0.4375$, $z/\delta_0 = 0$. High values of the correlation are observed around every multiple of $\Delta tu_\infty / \delta_0 \approx 5.0$, which suggests that these two signals are slightly correlated to each other at a frequency at $f\delta_0/u_\infty \approx 0.2$. In terms of correlation coefficients between reattachment location and bubble size, Fig. 15(b), there is strong positive and immediate connections between them with a quasi period $\Delta tu_\infty / \delta_0 \approx 40.0$. Therefore, the area of the separation bubble increases when the reattachment location moves downstream, and vice versa. This confirms that the low frequency ($f\delta_0/u_\infty \approx 0.025$) appears to originate from the breathing motion of the separation bubble. Concerning the connections between reattachment and shock location, they are obviously in the phase but with a slight time delay around $\Delta tu_\infty / \delta_0 \approx 6.1$. Physically, when the reattachment location moves upstream, the shock location also moves upstream after $\Delta tu_\infty / \delta_0 \approx 6.1$. It can be explained that the reattachment shock shifts upstream because the reattachment-induced compression waves, which coalesce into the reattachment shock, move upstream. The slight time delay is due to the wave propagation speed and probes causality. It should be noted that the sensitivity of above statistical correlations to the number of samples was verified by calculating the cross-correlation coefficients with half of the total time samples.

E. Dynamic mode decomposition

The above spectral and statistical analysis provides a first characterization of the unsteady features of the interactions and statistical links between them. To better decouple various frequency dynamics and further validate our obtained results, a modal decomposition of the flow field is carried out based on dynamic mode decomposition (DMD). DMD was first proposed by Schmid [43] as a numerical tool to identify the most important dynamic information of time sequential data from the flow field. Basically, given an equal-interval time series of data, DMD transforms this dynamic system into a set of modes, each of which is associated with a single orthogonal frequency behavior whose dynamics is governed by the corresponding eigenvalue. This algorithm has been widely applied for diverse flow problems, such as the transition mechanism from laminar to turbulent flow [44], unsteadiness of the SWBLI [25], and the identification of coherent vortex structures [45].

The current DMD analysis is based on 700 snapshots of the spanwise-averaged flow field (covering the time interval $tu_\infty / \delta_0 = 800 \sim 1150$) at a sampling frequency $f_s \delta_0 / u_\infty = 2$, which yields a frequency resolution of $2.9 \times 10^{-3} < St_{\delta_0} < 1$. In Fig. 16(a), we provide the eigenvalue spectrum resulting from the standard DMD. The input snapshots are real numbers while the computed modes appear as complex conjugate pairs, which results in a symmetric spectrum. The magnitudes of the corresponding DMD modes are shown in Fig. 16(b) for the positive frequencies. All the magnitudes are normalized by the maximum magnitude. This is a statistically stationary system since all of the eigenvalues are distributed near the unit circle $|\mu_i| = 1$, which means the snapshots sequence falls in an attracting set [46].

The sparsity-promoting DMD (SPDMD) [47] is employed to select the dynamically important modes. This method picks modes based on their contribution to a reproduction of the original

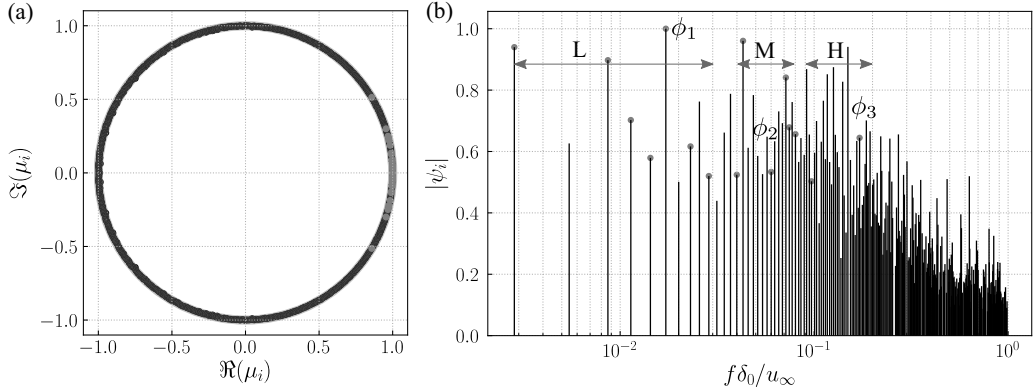


FIG. 16. (a) Eigenvalues spectrum from the standard DMD algorithm (b) Normalized magnitudes of all the DMD modes with positive frequency (● illustrates the most important 15 pairs of modes calculated by SPDMD).

dynamic system over the given time interval. By taking the positive regularization parameter equal to 780, we obtained the 15 pairs of modes that are indicated by the gray solid circles in Fig. 16. They are considered to be the most dynamically important modes and have the most significant influence on data sequences. These modes can be categorized as three sets based on their main flow structures and frequency range, with $0.003 \leq f\delta_0/u_\infty \leq 0.029$, $0.04 \leq f\delta_0/u_\infty \leq 0.08$, and $0.09 \leq f\delta_0/u_\infty \leq 0.20$, respectively. These frequency ranges have been indicated in Fig. 16(b) and labeled as L, M, H, which stands for low, medium, and high frequency. The frequencies of dominant modes are seen to be consistent with our previous spectral and statistical analysis in the preceding section.

For the branch with lower frequencies, we choose the mode with frequency $f\delta_0/u_\infty = 0.017$, indicated as mode ϕ_1 , to scrutinize the flow dynamics. The selected modes in the other two branches are labeled as mode ϕ_2 ($f\delta_0/u_\infty = 0.06$) and ϕ_3 ($f\delta_0/u_\infty = 0.172$). In Figs. 17, 18, and 19, the real and imaginary part of these modes illustrating the contour of streamwise velocity and pressure fluctuations are shown. To assist interpretation, we also reconstructed the real-valued

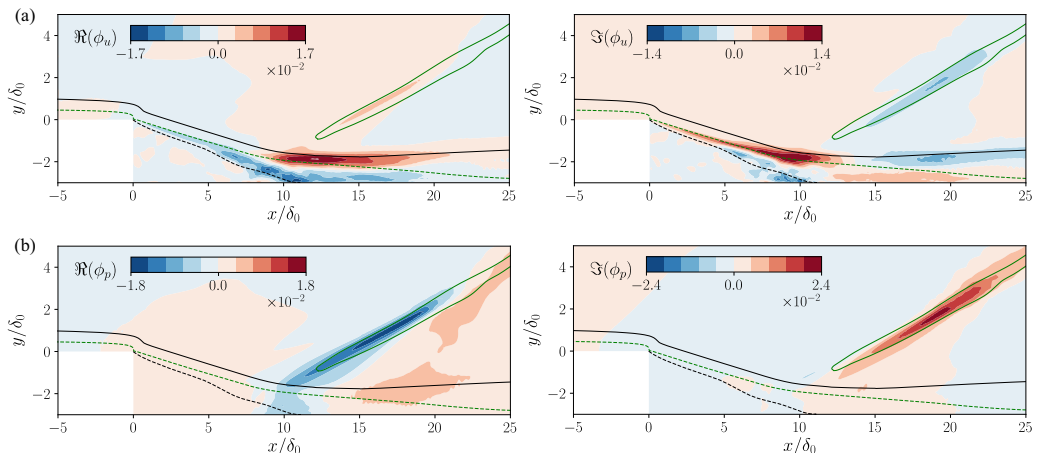


FIG. 17. Real and imaginary part of DMD mode ϕ_1 indicating contours of modal (a) streamwise velocity and (b) pressure fluctuations. The green solid and dashed lines indicate the mean reattachment shock and sonic line. The black solid and dashed lines signify the boundary layer edge and dividing line.

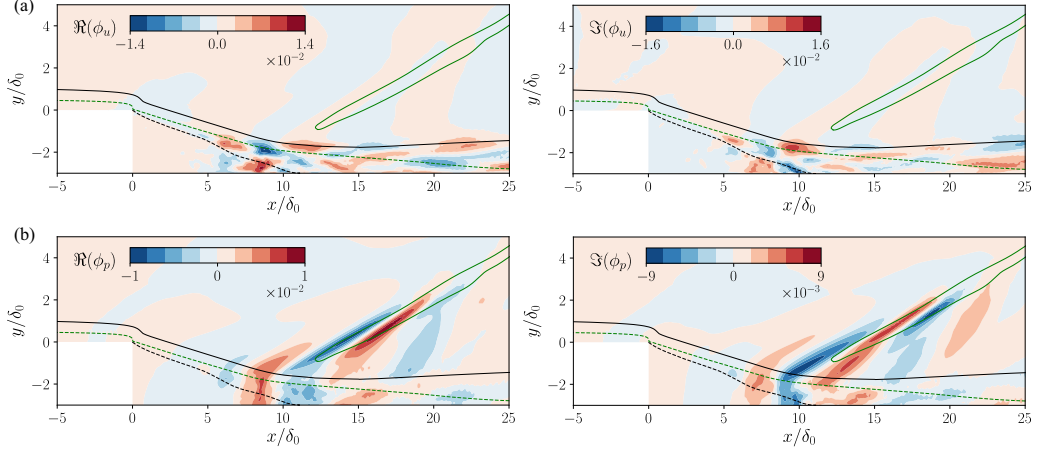


FIG. 18. Real and Imaginary part of DMD mode ϕ_2 indicating contours of modal (a) streamwise velocity fluctuations and (b) pressure fluctuations. The green solid and dashed lines indicate the mean reattachment shock and sonic line. The black solid and dashed lines signify the boundary layer edge and dividing line.

flow field of the individual modes by superimposing the fluctuations of each mode ϕ_i onto the mean flow ϕ_m , formulated as $q(x, t) = \phi_m + a_f \cdot \Re\{\alpha_i \phi_i e^{i\omega_i t}\}$, to examine the dynamical behavior represented by every mode, where α_i and a_f are the amplitude and optional amplification factor of the corresponding mode ϕ_i . In the following analysis, these amplification factors are $a_f = 10$ for the velocity fluctuations and $a_f = 90$ for pressure disturbance for all the modes to have a distinguishing visualization. Animations of the individual modes with the modulation of the mean flow are provided as the Supplemental Material online [48–50] and are helpful for the following discussion.

The lower frequency mode ϕ_1 falls into the frequency of the breathing motion of the separation bubble, which is the reason that high fluctuations of the streamwise velocity are distributed along the dividing line as a consequence of the flapping of the shear layer, shown in Fig. 17(a). In addition,

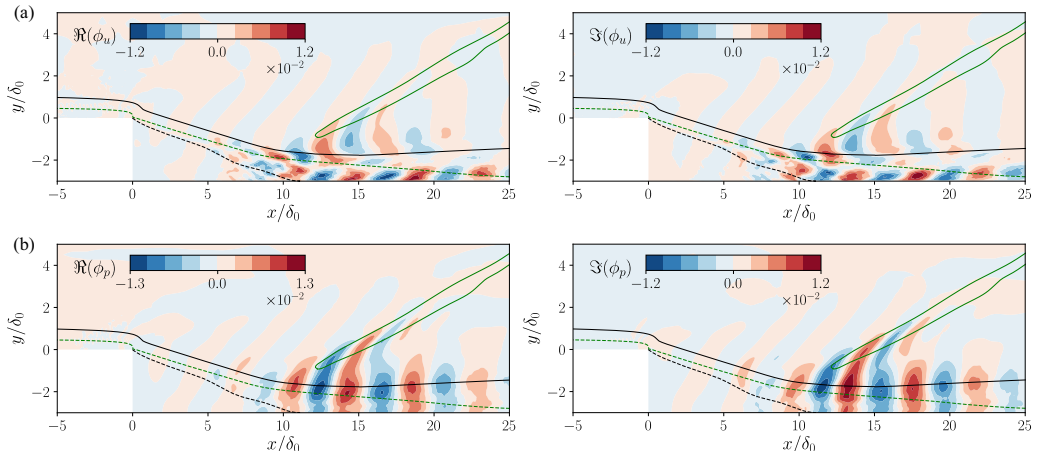


FIG. 19. Real and Imaginary part of DMD mode ϕ_3 indicating contours of modal (a) streamwise velocity fluctuations and (b) pressure fluctuations. The green solid and dashed lines indicate the mean reattachment shock and sonic line. The black solid and dashed lines signify the boundary layer edge and dividing line.

strong pressure fluctuations are observed along the reattachment shock in Fig. 17(b) due to flapping motion of the shock wave, which is caused by the contraction and dilatation of separation bubble. Hence, we conclude that this mode involves a breathing behavior of the separation bubble and concurrent streamwise motion of the shock wave system (can be seen clearly from the Supplemental Material online [48]).

The contours of mode ϕ_2 show strong streamwise velocity fluctuations around the reattachment location, see Fig. 18(a), which illustrates the large vortices originating in the shear layer. These vortices rapidly decay in downstream turbulent boundary layer, indicated by the low levels of the streamwise velocity fluctuations. Additionally, the reattachment compression and convection of large vortices produce high pressure fluctuations in the supersonic part along the reattachment shock, as shown in Fig. 18(b). A shock wrinkling dynamics is observed in the transient process of mode ϕ_2 , shown in the online animations [49]. The corrugation of the shock is a result of the interaction between the large coherent vortices and the reattachment compression. Similar results have been reported in the LES of an incident shock wave and boundary layer interactions by Pasquariello *et al.* [24].

Considering mode ϕ_3 in Fig. 19, we find alternative high positive and negative fluctuations along the streamwise direction both in streamwise velocity and pressure contour. The frequency of mode ϕ_3 is $f\delta_0/u_\infty = 0.172$, which is close to the characteristic frequency of the K-H vortex based on the spectral analysis. The traveling of K-H vortices induces eddy Mach waves in the supersonic portion of the flow field. From the temporal evolution of this mode (see online animations [50]), we can clearly observe the shedding of the K-H vortices with a relatively steady intensity along the streamwise direction and the propagation of Mach waves along the reattachment shock. Therefore, we consider that this mode is associated with the convection of the K-H vortices.

Based on the above analysis, the unsteady motions of the interacting flow field contain three types of dynamic behavior. The lower frequency branch ($0.003 \leq f\delta_0/u_\infty \leq 0.03$) describes a flow modulation that involves the breathing motion of shock and separation bubble system; the medium-frequency ($0.04 \leq f\delta_0/u_\infty \leq 0.08$) modes relate to the reattachment compression; while the higher-frequency part ($0.09 \leq f\delta_0/u_\infty \leq 0.20$) is associated with the convection of K-H vortices and induced Mach waves.

IV. CONCLUSIONS

We numerically investigated the dynamics of a BFS in a laminar backward-facing step flow at $Ma = 1.7$ and $Re_{\delta_0} = 13718$, with special attention on the laminar-to-turbulent transition mechanism and the global unsteady behavior. The mean flow shows that the boundary layer is turbulent behind the reattachment location. The instantaneous flow visualizations provide a clear view of the transition process, which is summarized in the schematic drawing in Fig. 20. Five distinct stages are identified in the transition process. At first stage, upon separation a quasisteady two-dimensional shear layer is formed due to the velocity difference of the flow on both sides of the separation line. Then clockwise rotating spanwise vortices are induced by the K-H instability with a frequency of $f\delta_0/u_\infty \approx 0.2$.

These K-H vortices grow rapidly and are subsequently deforming as a result of the ejection from the horseshoe vortices below as the free shear flow travels downstream in the second stage. The wavy K-H vortices have different traveling velocity in the spanwise direction and thus spanwise modulation occurs (third stage), which reduces the frequency of the breathing separation bubble to $f\delta_0/u_\infty \approx 0.02$. The high-speed parts develop into the head of Λ -shaped vortex and the low-speed parts develop into the legs parts due to the secondary instability. At the fourth stage, the large coherent vortices break down into several small Λ -shaped vortices caused by the streamwise stretching of vortices and the reattachment. The convection of the coherent structure and induced compression waves have an intermediate frequency with $\delta_0/u_\infty \approx 0.06$. Then the small vortices roll up and develop into larger hairpin vortices in the last phase, which is the indicator of the turbulent flow. The transition to turbulence is almost completed with the appearance of turbulent streaks.

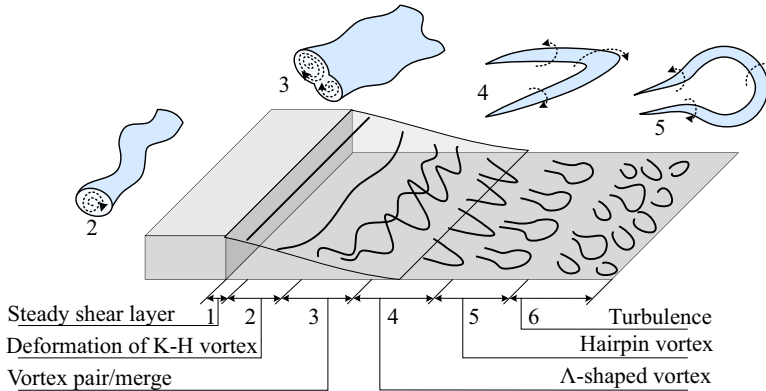


FIG. 20. Conceptual model of the transition process in the supersonic BFS.

Given the rapid modal growth of the disturbances behind the step and high levels of amplitudes, we believe the nonlinear behavior is significant in the transition process, which involves the modal growth of K-H and secondary instability, vortices breakdown and eventually fully developed turbulence, in the current case. The spectral and statistical analysis associates the flow phenomena with the unsteady behavior at different frequencies. The low-frequency breathing motions of the separation bubble exists in the whole transition process. However, the K-H instability seems to take the lead in the second stage and secondary instability in the third stage. We infer that the reattachment events and the oscillation of the shock appear to accelerate the transition process in the fourth stage.

The unsteadiness of the interacting system is characterized by a modulation of a broadband frequency dynamics. By means of SPDM, we further extracted the most important modes representing the dynamics of the flow field that are characteristic for specific frequency ranges. The flapping motion of the shock and separation bubble is associated with a lower frequency centered at $f\delta_0/u_\infty = 0.017$. The medium frequency mode ($f\delta_0/u_\infty = 0.06$) is related to the large coherent vortex shedding around the reattachment location and the wrinkling behavior of the shock, while the higher frequency mode ($f\delta_0/u_\infty = 0.172$) is associated with the traveling of K-H vortices and induced Mach waves. Flow reconstruction based on the selected DMD modes further elucidates the dynamic behavior of the interaction system.

ACKNOWLEDGMENTS

This work was carried out on the Dutch national e-infrastructure with the support of SURF Cooperative as part of Project No. 36790. The authors appreciate the facility and service provided by SURF.

-
- [1] R. Friedrich and M. Arnal, Analysing turbulent backward-facing step flow with the lowpass-filtered Navier-Stokes equations, *J. Wind Eng. Ind. Aerodyn.* **35**, 101 (1990).
 - [2] J. Kostas, J. Soria, and M. Chong, Particle image velocimetry measurements of a backward-facing step flow, *Exp. Fluids* **33**, 838 (2002).
 - [3] H. M. Blackburn, D. Barkley, and S. J. Sherwin, Convective instability and transient growth in flow over a backward-facing step, *J. Fluid Mech.* **603**, 271 (2008).
 - [4] D. Lanzerstorfer and H. C. Kuhlmann, Three-dimensional instability of the flow over a forward-facing step, *J. Fluid Mech.* **695**, 390 (2012).

- [5] P. T. Williams and A. J. Baker, Numerical simulations of laminar flow over a 3D backward-facing step, *Int. J. Numer. Methods Fluids* **24**, 1159 (1997).
- [6] H. P. Rani, T. W. H. Sheu, and E. S. F. Tsai, Eddy structures in a transitional backward-facing step flow, *J. Fluid Mech.* **588**, 43 (2007).
- [7] D. Lanzerstorfer and H. C. Kuhlmann, Global stability of the two-dimensional flow over a backward-facing step, *J. Fluid Mech.* **693**, 1 (2012).
- [8] C. E. Tinney and L. S. Ukeiley, A study of a 3D double backward-facing step, *Exp. Fluids* **47**, 427 (2009).
- [9] G. T. Duncan Jr, The effects of step excrescences on swept-wing boundary-layer transition, Ph.D. thesis, Texas A & M University, 2014.
- [10] X. Ma and A. Schröder, Analysis of flapping motion of reattaching shear layer behind a two-dimensional backward-facing step, *Phys. Fluids* **29**, 115104 (2017).
- [11] F. Schäfer, M. Breuer, and F. Durst, The dynamics of the transitional flow over a backward-facing step, *J. Fluid Mech.* **623**, 85 (2009).
- [12] J. L. Eppink, R. W. Wlezien, R. A. King, and M. Choudhari, Interaction of a backward-facing step and crossflow instabilities in boundary-layer transition, *AIAA J.* **56**, 497 (2017).
- [13] P. G. Spazzini, G. Iuso, M. Onorato, N. Zurlo, and G. M. Di Cicca, Unsteady behavior of back-facing step flow, *Exp. Fluids* **30**, 551 (2001).
- [14] M. W. Tufts, Computational investigation of sensitivity of the crossflow instability to two-dimensional surface imperfections, Ph.D. thesis, Texas A&M University, 2015.
- [15] P. Balakumar, R. A. King, and J. L. Eppink, Effects of forward and backward facing steps on the crossflow receptivity and stability in supersonic boundary layers, in *Proceedings of the 44th AIAA Fluid Dynamics Conference AIAA Aviation Forum* (AIAA 2014-2639, Atlanta, GA, 2014).
- [16] J. Tihon, J. Legrand, and P. Legentilhomme, Near-wall investigation of backward-facing step flows, *Exp. Fluids* **31**, 484 (2001).
- [17] A. Sriram and D. Chakraborty, Numerical exploration of staged transverse injection into confined supersonic, *Def. Sci. J.* **61**, 3 (2011).
- [18] Z. Chen, S. H. Yi, L. He, L. F. Tian, and Y. Zhu, An experimental study on fine structures of supersonic laminar/turbulent flow over a backward-facing step based on NPLS, *Chinese Sci. Bull.* **57**, 584 (2012).
- [19] Y. Zhu, S. Yi, D. Gang, and L. He, Visualisation on supersonic flow over backward-facing step with or without roughness, *J. Turbul.* **16**, 633 (2015).
- [20] I. Bolgar, S. Scharnowski, and C. J. Kähler, The effect of the Mach number on a turbulent backward-facing step flow, *Flow, Turbul. Combust.* **101**, 653 (2018).
- [21] S. Hickel, C. P. Egerer, and J. Larsson, Subgrid-scale modeling for implicit large eddy simulation of compressible flows and shock-turbulence interaction, *Phys. Fluids* **26**, 106101 (2014).
- [22] S. Hickel, N. A. Adams, and J. A. Domaradzki, An adaptive local deconvolution method for implicit LES, *J. Comput. Phys.* **213**, 413 (2006).
- [23] S. Gottlieb and C.-W. Shu, Total variation diminishing Runge-Kutta schemes, *Math. Comput.* **67**, 73 (1998).
- [24] V. Pasquariello, S. Hickel, and N. A. Adams, Unsteady effects of strong shock-wave/boundary-layer interaction at high Reynolds number, *J. Fluid Mech.* **823**, 617 (2017).
- [25] M. Grilli, P. J. Schmid, S. Hickel, and N. A. Adams, Analysis of unsteady behavior in shockwave turbulent boundary layer interaction, *J. Fluid Mech.* **700**, 16 (2012).
- [26] J. Mattheis and S. Hickel, On the transition between regular and irregular shock patterns of shock-wave/boundary-layer interactions, *J. Fluid Mech.* **776**, 200 (2015).
- [27] P. Schlatter and R. Örlü, Assessment of direct numerical simulation data of turbulent boundary layers, *J. Fluid Mech.* **659**, 116 (2010).
- [28] H. Liu, B. Wang, Y. Guo, H. Zhang, and W. Lin, Effects of inflow mach number and step height on supersonic flows over a backward-facing step, *Adv. Mech. Eng.* **2013**, 147916 (2013).
- [29] A. Karimi, S. D. Wijeyakulasuriya, and M. R. Nalim, Numerical study of supersonic flow over backward-facing step for scramjet application, in *Proceedings of the 48th AIAA/ASME/SAE/ASEE Joint Propulsion Conference & Exhibition*, AIAA-2012-4001 (2012).

- [30] J. H. Nie and B. F. Armaly, Reverse flow regions in three-dimensional backward-facing step flow, *Int. J. Heat Mass Transf.* **47**, 4713 (2004).
- [31] J. Délery, J. G. Marvin, and E. Reshotko, Shock-wave boundary layer interactions, Technical report (Advisory Group for Aerospace Research and Development, AGARD-AG-280, 1986).
- [32] T. Herbert, Secondary instability of boundary layers, *Annu. Rev. Fluid Mech.* **20**, 487 (1988).
- [33] W. W. Willmarth and S. S. Lu, Structure of the Reynolds stress near the wall, *J. Fluid Mech.* **55**, 65 (1972).
- [34] S. Cherubini, P. De Palma, J. C. Robinet, and A. Bottaro, The minimal seed of turbulent transition in the boundary layer, *J. Fluid Mech.* **689**, 221 (2011).
- [35] A. J. Smits and J. P. Dussauge, *Turbulent Shear Layers in Supersonic Flow* (Springer Science & Business Media, Berlin, 2006).
- [36] T. Herbert, Three-dimensional phenomena in the transitional flat-plate boundary layer, in *Proceedings of the AIAA 23rd Aerospace Science Meeting* (AIAA 85-0489, Reno, NV, 1985).
- [37] J. N. N. Murugan and R. N. N. Govardhan, Shock wave-boundary layer interaction in supersonic flow over a forward-facing step, *J. Fluid Mech.* **807**, 258 (2016).
- [38] S. Priebe and M. P. Martín, Low-frequency unsteadiness in shock wave-turbulent boundary layer interaction, *J. Fluid Mech.* **699**, 1 (2012).
- [39] Y. Na and P. Moin, Direct numerical simulation of a separated turbulent boundary layer, *J. Fluid Mech.* **374**, 379 (1998).
- [40] I. Lee and H. J. Sung, Multiple-arrayed pressure measurement for investigation of the unsteady flow structure of a reattaching shear layer, *J. Fluid Mech.* **463**, 377 (2002).
- [41] E. Touber and N. D. Sandham, Large-eddy simulation of low-frequency unsteadiness in a turbulent shock-induced separation bubble, *Theor. Comput. Fluid Dyn.* **23**, 79 (2009).
- [42] S. Priebe, J. H. Tu, C. W. Rowley, and M. P. Martín, Low-frequency dynamics in a shock-induced separated flow, *J. Fluid Mech.* **807**, 441 (2016).
- [43] P. J. Schmid, Dynamic mode decomposition of numerical and experimental data, *J. Fluid Mech.* **656**, 5 (2010).
- [44] T. Sayadi, P. Schmid, J. W. Nichols, and P. Moin, Dynamic mode decomposition of controlled H- and K-type transitions, *Cent. Turbul. Res. Annu. Res. Briefs* 189 (2013).
- [45] Q. Zhang, Y. Liu, and S. Wang, The identification of coherent structures using proper orthogonal decomposition and dynamic mode decomposition, *J. Fluid Struct.* **49**, 53 (2014).
- [46] C. W. Rowley, I. Mezić, S. Bagheri, P. Schlatter, and D. S. Henningson, Spectral analysis of nonlinear flows, *J. Fluid Mech.* **641**, 115 (2009).
- [47] M. R. Jovanović, P. J. Schmid, and J. W. Nichols, Sparsity-promoting dynamic mode decomposition, *Phys. Fluids* **26**, 24103 (2014).
- [48] See Supplemental Material at <http://link.aps.org/supplemental/10.1103/PhysRevFluids.4.103904> for the flow reconstruction from DMD mode ϕ_1 . The animation shows the contours of pressure gradient at 32 phase angles. The green solid and dashed lines indicate the mean reattachment shock and boundary layer edge. The white solid line is the instantaneous isoline of $u = 0$. The black solid and dashed lines denote the instantaneous isolines of $u' = 0.007$ and $u' = -0.007$. Same notations for other animations.
- [49] See Supplemental Material at <http://link.aps.org/supplemental/10.1103/PhysRevFluids.4.103904> for the flow reconstruction from DMD mode ϕ_2 with $u' = 0.003$ and $u' = -0.003$.
- [50] See Supplemental Material at <http://link.aps.org/supplemental/10.1103/PhysRevFluids.4.103904> for the flow reconstruction from DMD mode ϕ_3 with $u' = 0.004$ and $u' = -0.004$.